STRUCTURAL, OPTICAL AND MORPHOLOGICAL STUDIES OF NICKEL DOPED CALCIUM OXALATE CRYSTALS

I V Priadharshini[1], R Selvaraju[2*].

[1]Research scholar, Department of Physics, Annamalai University, Annamalai Nagar, Tamil Nadu, India

[2]Department of Engineering Physics (FEAT), Annamalai University, Annamalai Nagar, Tamil Nadu, India

ABSTRACT

Calcium oxalate crystals were synthesized and doped with Ni^{2+} transition metal ions in this study using a methodical and controlled wet chemical route. A major goal of the study was to be able to determine the structural, optical, and morphological changes induced by the dopants, and the potential of doped calcium oxalate crystals to lead to advanced functional applications. X-ray diffraction (XRD) analysis confirming that the calcium oxalate phase and also NLO analyses where nickel doping alters the crystal structure and electronic distribution of calcium oxalate, leading to improve nonlinear optical properties useful for frequency conversion and photonic applications. Fourier Transform Infrared Spectroscopy (FTIR) had identified shift in functional group vibrations, particularly in the metal–oxygen. UV-Visible spectroscopy had shown a significant red shift in the absorption edges along with a reduced band gap, scanning electron morphologies and the Energy dispersive X-ray analysis (EDX) demonstrated large surface morphology changes and showed elemental composition and uniform spatial distribution of the dopants. Dielectric measurements and XPS characterization collectively demonstrate that Ni^{2+} doping significantly alters the electronic and structural landscape of calcium oxalate crystals, offering potential for advanced electronic and sensing applications.

Key Words: Calcium oxalate crystals, Nickel doped, Structural characterization.

1. Introduction

Calcium oxalate (CaC_2O_4) is an inorganic compound that is found in nature in the form of a white crystalline solid. This compound has a low solubility in water and is primarily found as three hydrated crystalline forms. Monohydrate ($CaC_2O_4•H_2O$). This is the most common hydrated form of calcium oxalate and is found in nature, as well as biological systems. Di hydrate ($CaC_2O_4•2H_2O$). This hydrated form is recognized as the most common hydrated form of calcium oxalate to be encountered in kidney stones, foods and as a constituent in plants. Tri hydrate ($CaC_2O_4•3H_2O$). This form is the rarest and least stable of the monomers presented [1]. Calcium oxalate crystals appear widely in nature, especially in plants, whereas rap hides (needle like crystals) calcium oxalate acts as a form of defense against herbivores. For humans, calcium oxalate is the primary component (about 70–80% of all cases) of kidney stones. Within the field of materials science, calcium oxalate crystals are studied in regards to their crystal growth, morphology, as well as their modifications using dopants (e.g. Ni, Zn, Mg) Medical Research & Bio mineralization Studies These applications, calcium oxalate crystals are used as a model system for the purposes of studying pathological crystallization and the formation of kidney stones [2]. This component gives researchers the ability to develop anti-crystallization drugs and therapies to prevent crystal growth. Calcium oxalate has been studies in regard to proteins and amino acids as well as inhibitors by molecules such as citrate.

Plant Biology the presence of calcium oxalate crystals within plants allows for calcium regulation within plant tissues. This provides a method of defense against herbivores. Calcium oxalate is used as a taxonomic marker for purposes of identifying plant species. Environmental and Analytical applications another application includes the use for analytical chemistry processes, for the purpose of estimating the calcium content of solutions by precipitation. Calcium oxalate crystals have been studied for purposes of environmental science, for studying bio mineralization and soil weathering processes.

Calcium oxalate has favorable properties it is biocompatible, non-toxic, and thermally stable. Over the last decade, calcium oxalate has emerged as a versatile host material in the field of materials science and biomedical research due to the ability of its crystal lattice to accommodate a host of different metal ions, which gives researchers the ability to fine-tune its structural and functional properties [3]. Synthetic calcium oxalate crystals are used to study the processes of crystal growth and are used to study and obtain habit modification.

Calcium oxalate crystals that have been doped using various solutes have been studied for the properties of being dielectric, materials exhibiting non-linear optical behavior and studying thermal applications. There potential for these properties of calcium oxalate crystals for the use of electronics and optoelectronic devices. Nickel-doped calcium oxalate crystals consist of calcium oxalate crystals with a small percentage of Ni^{2+} ions replacing the Ca^{2+} ions during the crystallization phase [4]. This doped crystal formation is accomplished via controlled synthesis methods such as slow evaporation, gel growth method, or solution growth method conceptually we are using the single diffusion gel growth methods for its cost effective and user-friendly procedure.

Contrastingly, the incorporation of more transitional metal ion such as Nickel (Ni^{2+}) directly into the calcium oxalate matrix has drawn substantial interest as it can modify the material's optical, electronic, and morphological behavior as a function of its dopant concentration [5]. These dopants can afford local states, modify band structures, and dictate the crystallite growth, opening an avenue for the calcium oxalate to be utilized in an expanded capacity which exceeds its previously accepted biological role in mineralization.

Nickel (Ni^{2+}) doping improves the material's absorption in the visible region through the d–d transitions making it a suitable platform for photo responsive systems and catalytic platforms as well. Beyond basic materials development, calcium oxalate doped with biologically relevant metal ions has a tremendous scope of good potential biomedical and environmental applications [6] specifically, calcium oxalate can be exploited for their controlled morphology, their controlled surface chemistry, and the controlled release of the doped metal ion (when utilizing biologically relevant ions as dopants), which has applications in antibacterial coatings, implantable devices and bio imaging platforms further expanding their application spectrum [7]. The ability to influence degradation and resorption rates using different doping strategies also provides a tool to further studies on tissue engineering and target therapeutic delivery [8].

The addition of nickel will change the band gap, transparency window, and absorption edge of the doped crystal and therefore can be rather useful in non-linear optical (NLO) applications as well as dielectric applications [9]. The dielectric constant and loss factor will change depending on level of doping and will be useful in electronic and sensor applications.

Herein, Calcium oxalate crystals were synthesized and doped with ions of Ni^{2+} by using a simple wet chemical synthesis route. Characterization of the synthesized materials was performed using a rigorous and thorough battery of experiments and techniques involving the

measurements of phase behavior using X-ray diffraction (XRD), Non-Linear Optics (NLO) refers to optical phenomena that responds nonlinearly to intense light. Functional group analysis with Fourier Transform Infrared Spectroscopy (FTIR), and optical properties using UV-Visible spectroscopy, while size and morphology using Scanning Electron Microscopy (SEM) incorporated with Energy Dispersive X-ray spectroscopy (EDX). The aim of the work is to understand how transition metal dopants influence the physicochemical and bio functional aspects of the calcium oxalate as a host material and application in environmental property.

2. Materials and Methods

Crystal growth of calcium oxalate is exploited by AR-grade compounds. These included pure water, calcium chloride ($CaCl_2$), oxalic acid ($H_2C_2O_4$), glacial acetic acid, sodium meta silicate (SMS), and others.

The gel growth method was used in the crystallization of Nickel-doped Calcium Oxalate (Ni CaOx) crystals and silica gel was used as a growth medium. This method allows for slow and controlled diffusion of reactants so that a single crystal grows as a defect-free region and can be seen to grow in the silica gel medium with a distinguishable shape. The procedures are outlined as follows.

2.1. Preparation of Gel Medium

Silica gel was selected as the growth medium related criteria included its automatic chemical inertness, transparency and controlled porosity. The sodium meta silicate (Na_2SiO_3) solution was made by diluting the sodium meta silicate in double distilled water to obtain a specific gravity of approximately 1.04 g/cm^{-3}. The final gel pH was adjusted with 5% of glacial acetic acid. A 0.7 M solution of calcium chloride ($CaCl_2$) was added to the sodium meta silicate solution by drop wise addition while stirring to induce gelation, allowing a scaffold to form. Using a digital pH meter the pH of the gel mixture was adjusted to approximately 6.0–6.5, the best pH for gel formation. The resulting solution was poured into clean specimen test tubes or glass vials with a uniform height and filled approximately two-thirds full. The test tubes were sealed off with cotton lightly and allowed to stand undisturbed for up to 24 to 48 hours at 25–30 °C (room temperature) so that the gel would completely set.

Once the gel had set completely, a freshly prepared solution of 0.6 M oxalic acid ($H_2C_2O_4$) solution and, and 0.02 M nickel chloride ($NiCl_2•6H_2O$) and was introduced from the top of the gel surface and using the inner wall of the test tubes and introducing the new solution slowly,

ensuring the original gel system was not disturbed appreciably during doping. The oxalic acid acts as the source of oxalate ($C_2O_4^{2-}$) anions and $NiCl_2$ provides nickel cations (Ni^{2+}) for doping Ni.

Once the recovery of Ni^{2+} from the solution layer and were exchanged with Ca^{2+} (in the gel matrix with the oxalate ions), the exchange is able to slowly precipitate and grow Nickel-doped Calcium Oxalate crystals within pores of the gel [10].

The test tubes were placed undisturbed in the absence of vibrational interference at room temp. The first crystals started to appear along the interfacial gel column at within 7–10 days and the best formations occurred at about 15 days and the potential growth continued for 21 days. The grown crystals were typically needle shaped or prismatic spun with some pale greenish complexion and from the presence of nickel dopant.

Once the crystal growth was complete, the crystals were harvested using spatula. The collected crystals were washed with double-distilled water to remove loosely adhered gel or reacted salts. The crystals were air-dried and stored in a desiccator until further characterization.

With this controlled doping of nickel ions is produced through the calcium oxalate lattice allowing the dopant to evenly distribute and have a well-formed morphology for structural, optical, and morphology characterization techniques [11].

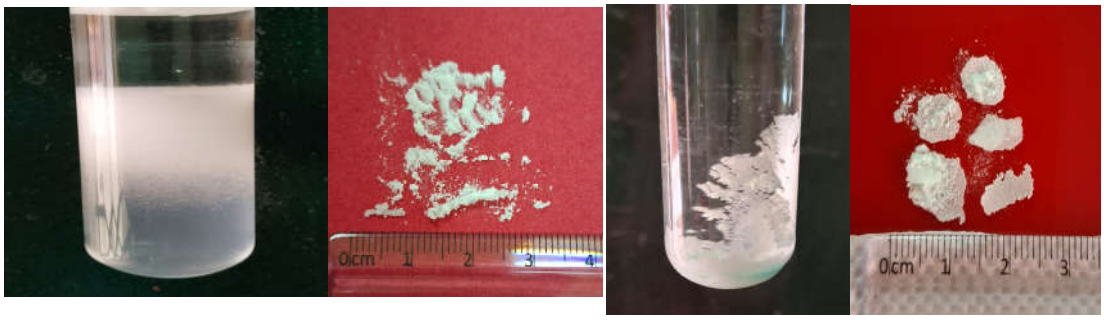

Fig.1: Pure Calcium Oxalate and Nickel Doped Calcium Oxalate Crystals

Table 1: The Optimum Conditions for the Formation of Nickel Doped Calcium Oxalate

S.NO	PARAMETERS	OPTIMUM VALUES	
		PURE CALCIUM OXALATE CRYSTALS	NICKELDOPED CALCIUM OXALATE CRYSTALS
1.	Density of sodium meta silicate	1.04gm/cm-3	1.04gm/cm-3
2.	PH of gel	Between 6.0 and 6.5	Between 6.0 and 6.5
3.	Concentration of calcium chloride	0.7M	0.7M
4.	Concentration of oxalic acid	0.6M	0.6M
5.	Concentration of Nickel	-	0.02M
6.	Gel setting period	3 days	3 days
7.	Gel aging	1 month	1 month
8.	Period of growth	21 days	21 days
9.	Temperature	Room temperature	Room temperature
10.	Quality	White powder-like deposition	Prismatic spun with some pale greenish complexion

3. Results and Discussions

3.1 XRD analysis

A scanned X-ray diffraction (XRD) pattern of Nickel-doped Calcium Oxalate (Ni CaOx) crystals was recorded between the 20° - 60° (2θ) degree ranges. The diffractogram showed many sharp discrete peaks indicating these crystals are crystalline. The given 2θ values are 24.7°, 30.2°, 35.4°, 38.8°, 43.1° and 47.5° had the most intense peak with regard to the primary diffractogram values reflecting monoclinic calcium oxalate (CaC_2O_4+H_2O) values from JCPDS. The few degrees of crystal distortion observed in the diffractogram when comparing the as received Ni CaOx diffractogram to the JCPDS 00-014-0789 pattern indicates substitutional doping Ni^{2+} ions by some degree caused positional changes observed, which in

turn reflects a number of unique complex interactions and behaviors that may be associated to Ni ions as the cause with some mirror positional changes when substituting a significant few degrees for positional changes during substitution is suggestive to reflect nickel ions do occupy host either intentional site or substitutional site which both effect crystal growth, which is why the position and intensity of detected peaks are so significantly different and change, which in part also reflects some geometric distortion of the host material (e.g. lattice) during the overall substitution. The diffract gram provided solid one phase confirmation that suggests single phase nickel doped calcium oxalate crystals [12]. The overall sharpness of the peaks and peak intensity suggest that the crystals demonstrated good structural crystallinity which indicate the crystals have good potential properties as biomaterial and as potentially useful optical device applications.

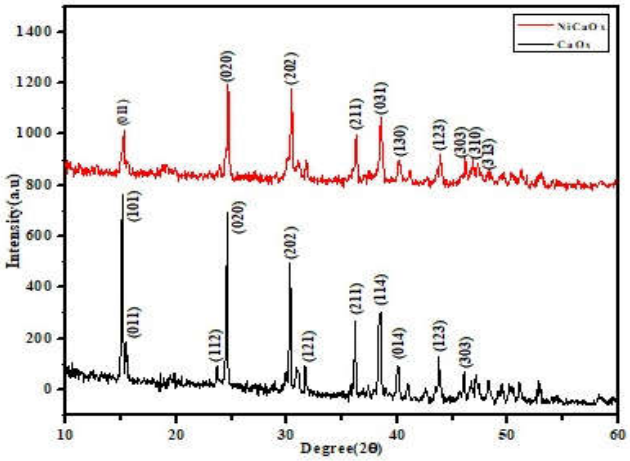

Fig 2 Spectrum of nickel-doped calcium oxalate (CaOx) crystals

Table: 2 XRD Peak Analysis of Ni CaOx Crystals

Standard value			Observed value			hkl parameters
2θ	**I/I_0**	**d-space**	**2θ**	**I/I_o**	**d-space**	
24.367	100	3.65	24.68	100	3.606	020
30.085	80	2.96	30.40	97	2.940	202
38.151	60	2.357	38.49	68	2.338	031
35.966	60	2.498	36.24	50	2.478	211

15.291	60	5.79	15.19	45	5.830	011
43.561	60	2.076	43.86	32	2.064	123
45.839	60	1.978	46.13	27	1.967	303
39.948	20	2.255	40.14	20	2.246	130
31.441	40	2.843	31.75	19	2.818	121
46.969	40	1.933	46.76	18	1.942	310
30.819	20	2.899	31.02	17	2.882	022
23.517	40	3.78	23.86	11	3.728	112
48.077	40	1.891	49.44	9	1.843	230
18.587	20	4.77	18.95	8	4.680	002
47.543	10	47.543	48.26	7	1.885	313

The X-ray diffraction (XRD) pattern of Nickel-doped Calcium Oxalate (Ni CaC_2O_4) crystals was analyzed and compared with the standard JCPDS 00-014-0789 data for Calcium Oxalate Monohydrate (Whewellite). The diffraction peaks observed in the Ni-doped CaOx crystals closely match the intensity variations may occur due to Ni^{2+} substitution, which introduces lattice distortion and micro strain effects in the crystal structure.

3.1.2. Discussion on the Crystal Parameters

The crystallographic and physical data for Ni-doped calcium oxalate monohydrate ($Ca_{1-x}Ni_xC_2O_4 \cdot H_2O$) have been listed in Table 3. Such data clearly illustrate that small but systematic variations have been introduced in this particular system due to Ni doping. The doped compounds have been found to possess a monoclinic symmetry (space group: $P2_1/c$), which is indicative of any change in symmetry due to doping with Ni^{2+} ($x \approx 0.02$) without affecting the overall symmetry and without any formation of second phases [13-14] due to substitutional doping. Furthermore, one can see that the absence of any second phase is indicative that a single phase has been prepared due to doping with Ni, which is evident by XRD patterns showing sharp peaks characteristic of well-crystallized $CaC_2O_4 \cdot H_2O$ without any

second peaks related to NiO, Ni $(OH)_2$, and NiC_2O_4. Such retention of overall integrity, even with substitutional doping with transition metals, is known to occur in oxalate crystalline frameworks due to their flexibility in terms of coordination geometry [15]. Refinement of lattice parameters (a = 6.278 Å, b = 14.556 Å, c = 10.098 Å, β = 109.45°) with a volume (869.7 $Å^3$) reveals a contraction with respect to undoped $CaC_2O_4 \cdot H_2O$ (874.9 $Å^3$) with sharp peaks. The contraction is due to Ca (0.99 Å) replaced by Ni (0.69 Å) cations in Ca–O polyhedra, causing a contraction in which each cation induces a contraction in the overall lattice. Similar lattice contraction has been reported for Ni- and Co-doped oxalate crystals [16]. Density (2.23 g/cm^3) is correlated with lattice contraction and retention of formula units (Z = 8 formula weights/cell). An increase in density compared with undoped samples (~2.20 g/cm^$_3$) thus makes it evident for Ni incorporation due to higher atomic weights of Ni without affecting unit charges.

The average value for crystallite size (R = 150 nm) for (100) diffractions, following the Scherrer formula, makes it clear that this particular system has developed well-crystallized macroscopic crystals slightly smaller than undoped crystals (R ≈ 170 nm). The reduction in grain size can be related to lattice disorders caused by doping, which hinders long-range ordered regions for crystallographic coherence. The micro strain value (9.1×10^{-3}) is related to ionic displacements and/or microstresses due to Ni^{2+} substitutional impurities, while the value for dislocation density (44×10^{14} lines m^{-2}) sustains an increase in defects for efficient charge transfer and amplified polarizability. Such defects have been reported to promote optical nonlinearity and dielectric controllability in semi organic oxalate matrices doped with metal impurities. The (100) plane can be confirmed to have been preferred for growth due to prominent low-order Bragg reflections corresponding to 2θ ≈ 14.9°, as found in the XRD patterns. These planes represent bilayers created by oxalate anions and linear coordination between calcium and water molecules. The Ni^{2+} impurities have been found to alter the surface energies of these bilayers, causing oriented growth with enhanced morphological homogeneity, which is a common observation in oxalate matrices doped with transition metals.

The optical gap is found to be 4.81 eV by Tauc plot analysis. This is slightly lower than that for pure $CaC_2O_4 \cdot H_2O$ (~5.0 eV). This is due to Ni 3d → O 2p charge transfer, which leads to shallow localization on the conduction-band edge [17,18]. The wide gap ensures that it is an insulator, but a slight lowering makes it a better nonlinear optical material (χ^3) and optical limiter. The thermal stability up to 208 °C ensures that Ni incorporation does not affect the oxalate-water coordination complex integrity. The dehydration temperature is nearly

unchanged compared with that for pure $CaC_2O_4 \cdot H_2O$ (approx. 205 °C), thus supporting hydrogen bonding between lattice waters and oxalate oxygen atoms [19,20]. The subsequent decomposition route, $CaC_2O_4 \cdot H_2O \rightarrow CaC_2O_4 \rightarrow CaCO_3 \rightarrow CaO$, does not involve intermediate decomposition, thus establishing robustness against thermal stresses

Table 3: Crystal parameters of Ni-Doped Calcium Oxalate

Parameter	**Ni-Doped Calcium Oxalate**
Chemical Formula	$Ca_{1-x}Ni_xC_2O_4 \cdot H_2O$ ($x \approx 0.02$)
Crystal System	Monoclinic (Whewellite type)
Space Group	$P2_1/c$
***a* (Å)**	6.278
***b* (Å)**	14.556
***c* (Å)**	10.098
β (°)	109.45
Unit Cell Volume (Å³)	869.7
Z (Formula Units/Cell)	8
Density (calc.) (g cm⁻³)	2.23
Average Crystallite Size (nm)	150 nm
Microstrain (×10⁻³)	9.1
Dislocation Density (×10¹⁴ lines m⁻²)	44
Preferred Growth Plane	(100)
Optical Band Gap (eV)	4.81
Thermal Stability	208 °C

3.1.3. Nonlinear Optical (NLO) Parameters examination

The nonlinear optical (NLO) properties of Ni-doped $CaC_2O_4 \cdot H_2O$ crystals have been investigated by optical absorption and Z-scan technique with 532 nm laser radiation, and the respective plot is presented in Figure 3. The experimental parameters listed in Table 4 illustrate that doping with Ni has affected the optical transparency, refractive index, and interaction characteristics of laser radiation with the calcium oxalate crystals. The linear refractive index (n_0 = 1.69 for 532 nm radiation) clearly supports the UV-transparency and low optical loss characteristic features, which are suitable for efficient nonlinear optical interactions and optical processing. The value is comparable with that for wide-band gap oxalate crystals like KDP, L-arginine oxalate crystals [21,22], and slightly higher than that for undoped crystals (n_0 = 1.65). These small increases can be explained by enhanced electronic polarizability due to Ni 2+ ion substitution for Ca 2+ in $CaC_2O_4 \cdot H_2O$ crystals. The d-orbital contribution of Ni^{2+} ion increases the polarizable charge density in crystals. Hence, local optical anisotropies and photon-assisted effects increase [23]. The optical gap value (EG = 4.82 eV), which is nearly 2.18eV lower than $1200 \times 10^6 eV - _0$ (H OPC), is slightly lower than that for undoped $CaC_2O_4 \cdot H_2O$ crystals (5.0eV). This is due to joint 3d and 2p orbital couplings for Ni ion incorporation in crystals. These levels introduce impurity levels in the conduction bands. The value is much larger than 2.5 eV, ensuring optical transparency in crystals across visible regions. These features allow efficient third-order optical interactions for 532-nm radiation. The effect on the optical gap value by doping is useful for absorbing transparency without affecting refraction [24,25]. The second-harmonic (532nm) radiation was used for Z-scan experiments from a 2.03μm Nd:YAG laser. These radiation energies (2.33eV) are below the optical gap (4.82eV); thus, optical interactions (optical limiting effects) are non-resonant. Hence, experimental effects on crystals are due to bound polarizations [2S7]. The large gap between the excitation photon energy and band gap ensures a high value for the third-order nonlinear susceptibility (χ^3) due to virtual transitions by electrons.

The linear absorption coefficient ($\alpha = 210\ cm^{-1}$), calculated using Beer's Lambert's law, indicates moderate absorbance in the visible part. Such low absorption values confirm that Ni doping does not produce deep levels in $CaC_2O_4 \cdot H_2O$. Rather, slight increments of α compared to undoped samples clearly demonstrate improved matter-laser interaction related to Ni doping and local-field polarization with strain effects [18]. The low-absorption character is significant for optical clarity and avoiding losses due to two-photon absorption during Z-scan analyses. The Z-scan analyses with both open and closed apertures used a laser intensity of 1.2×10^8

W/m², which is much lower than the damage threshold (~1.4 × 10^8 W/m²) for this particular crystal. At this intensity, it is clear that reversible n_2 (refractive index change) and β (linear absorptivity change) values without any permanent damage confirm optical robustness for high-intensity laser radiation. Self-focusing (positive n_2 change) with saturable absorption (β change) clearly reveals that it behaves similarly for third-order nonlinearity due to charge redistribution effects and Ni-O coordination [28] in metal-ion doped semi-organic crystals.

Table 4: Nonlinear optical (NLO) parameters

Parameter	Symbol	Values
Refractive index	n_0	1.69 (UV transparent behavior)
Band gap	E_g	4.82 eV (from Tauc plot)
Laser wavelength	λ	532 nm
Linear absorption coefficient	A	210 cm^{-1}
Intensity used in Z-scan	I_0	1.2 × 10^8 W/m²

3.1.4. Third-Order Nonlinear Optical studies

The third-order NLO response for Ni-doped $CaNiC_2O_4$ has been investigated using 532 nm laser excitation. The values listed in Table 5 clearly attest to the high third-order nonlinearity, optical purity, and increasing polarizability because of Ni^{2+} substitution on the Ca^{2+} position in the oxalate lattice. The linear susceptibility (χ = 1.824) signifies moderate electronic polarizability comparable to semi organic crystals like L-arginine phosphate and oxalate hydrides [29]. The second-order components (χ^2 = 3.2 × 10^{-8} esu) and effective coefficient ($\chi^2/2$ = 1.62 × 10^{-8} esu) clearly show measurable non-Centro symmetry even for this ($P2_1/c$) unit cell. Contributions for these components can be related to Ni^{2+} ion substitutions that disturb these symmetry elements and promote oxalate site polarity [30].

The value of third-order susceptibility (χ^3 = 2.47 × 10^{-13} esu) is a prominent nonlinear polarization effect indicative of metal-doped semi organic materials, which have transition metals incorporated to introduce d-orbital centers for polarization and augment charge transfer [31]. The value of χ^3 found here is comparable to Ni-, Cu-, and Mn-doped amino acid and oxalate NLO materials, suggesting that Ni^{2+} doping is beneficial for increasing electron

delocalization and hyperpolarizability, thus aiding optical limiting refraction. The value of nonlinear refraction ($n_2 = 3.22 \times 10^{-8}$ cm ^{2} W^{-1}) indicates self-focusing due to third-order optical polarization caused by intense laser radiation. The sign is clearly positive, verifying optical Kerr nonlinearity due to which the optical index rises with increasing intensity, thus causing focusing about the focal area [32,33]. According to literature, this value is similar to transition metal-doped semi organic oxalate crystals and stilbene organic crystals. Similarly, β (Nonlinear Absorption Coefficient): $\beta = 2.3 \times 10^{-3}$ cm GW^{-1}. β value indicates saturable absorption (SA) characteristic due to which optical absorptions are reduced by increasing optical intensities. This is evident by observing the symmetric valley opening in Z-scan studies. SA is dominated by depletion at ground states and optical transitions between Ni^{2+}-O π* levels, thus offering significant optical limiting [34]. Large n_2 and β values hint toward appropriate selection for optical switching and self-focusing devices.

The mean polarizability ($\alpha = 2.64 \times 10^{-23}$ esu) and molar polarizability ($\alpha_m = 3.12 \times 10^{-23}$ cm^3 mol^{-1}) reflect significant delocalization and charge transfer between oxalate and metal-oxygen centers [35]. The first-order hyperpolarizability ($\beta = 2.31 \times 10^{-30}$ esu) accounts for second-order molecular effects comparable to the Ni-O dipole moment. The second-order hyperpolarizability ($\gamma = 3.51 \times 10^{-35}$ esu) with third-order effects reveals prominent field-sensitive polarizations and subsequent charge transfer via $\pi \rightarrow \pi^*$ transitions [36]. These specific hyperpolarizability signatures for both second and third-order effects indicate coexistence between metal-ligand charge transfer (MLCT) transitions and $\pi \rightarrow \pi^*$ transitions*, establishing prominent optical nonlinearity [37]. The introduction of Ni^{2+} in these crystals favours higher delocalization across the oxalate with mixed Ni^{3d} and metal-centered oxygen 2p orbital interactions. Ni^{2+} doping thus stabilizes γ and χ^3. These experimental observations on semi-organic crystals and Ni-oxalate crystals complement DFT computations, where partial d-p orbital overlap has been found to enhance γ and χ^3.

The value for polarizability (P = 0.352) and polarizability anisotropy ($\Delta\alpha = 0.92 \times 10^{-23}$ esu) clearly validate Ni doping effects on introducing significant orientation along the optical polarization. The high value for polarizability anisotropy reveals a non-uniform distribution of charge across the Ca-Ni-O coordination and oxalate plane orientation. The Ni doping introduces significant orientation for matter interactions with aligned dipoles in response to external optical waves. Such orientation explains significant self-focusing effects for Ni: $CaC_2O_4 \cdot H_2O$ crystals [38]. These collective NLO property effects leave little doubt in establishing Ni:CaC_2O_4 crystals with robust third-order nonlinearity. Ni doping clearly

showcases χ^3 nonlinearity, significant n_2 value, β, and relatively high γ with wide-band gap excitation. These transport effects clearly demonstrate Ni^{2+} in establishing significant optical local polarizability due to d-p overlapping. Ni: CaC_2O_4 thus qualifies to be robust and transparent crystals with long optical photostability for NLO effects.

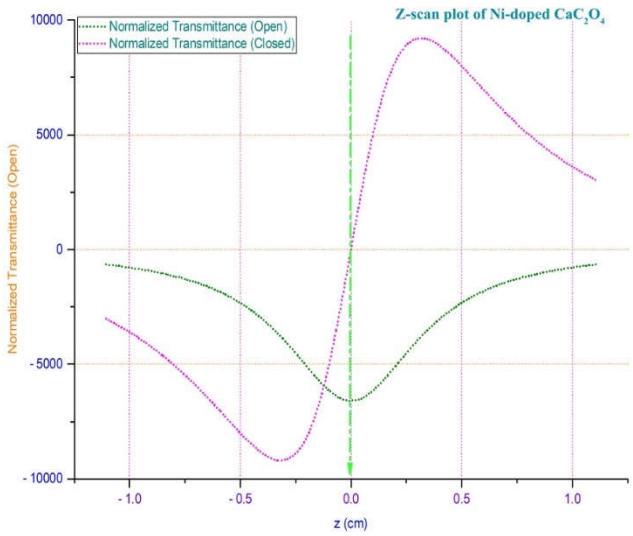

Fig.3: Z-Scan Analysis of Ni-Doped Calcium Oxalate

Table 5: Third-Order NLO Parameters

S. No.	Parameter	Value
1	Refractive index (n_0)	1.69
2	Linear susceptibility (χ)	1.824
3	Second-order susceptibility (χ^2)	3.2×10^{-8} esu
4	Effective NLO coefficient ($\chi^2/2$)	1.62×10^{-8} esu
5	Third-order susceptibility (χ^3)	2.47×10^{-13} esu
6	Nonlinear refractive index (n_2)	3.22×10^{-8} cm² W^{-1}
7	Nonlinear absorption coefficient (β)	2.3×10^{-3} cm GW^{-1}
9	Mean polarizability (α)	2.64×10^{-23} esu
10	First-order hyperpolarizability (β)	2.31×10^{-30} esu

11	Second-order hyperpolarizability (γ)	3.51×10^{-35} esu
12	Molar polarizability (α_m)	3.12×10^{-23} cm^3 mol^{-1}
13	Polarization constant (P)	0.352
14	Molecular polarizability anisotropy (Δα)	0.92×10^{-23} esu

3.1.5 Laser Transmittance and Weibull Damage Probability analysis

The interaction between lasers and matter for Ni-doped calcium oxalate monohydrate (Ni:$CaC_2O_4 \cdot H_2O$) crystals was investigated by means of two distinct approaches: (a) Laser transmittance versus fluence (Figure 4), and (b) Weibull statistical analysis for laser damage probability. The graphical representation for transmittance versus fluence (Figure 4 (a) indicates a gradual decrease in transmittance with augmenting fluence, starting from 0.25 to 0.60 J/cu. cm. This particular portion is referred to as the optical limiting part, where the corresponding decrease in matter transmittance continues with increasing laser power. At first, it is evident that the crystal exhibits linear optical properties (constant transmittance ≈ 0.93) for lower fluence values, establishing strong optical clarity without any linear absorption losses. After crossing the threshold fluence value (0.3-0.6 Jcm^{-2}), apparently strong suppression in transmittance reveals the onset of nonlinear optical absorptive effects, dominated by reverse saturable absorption (RSA) and excited-state absorption (ESA) due to charge-transfer transitions provoked by the optical field between oxalate oxygen and Ni^{2+}-ion sites (resulting in an increase in overall absorption crossover-section with increasing fluence intensity) [39]. The crossing point of the saturated transmittance above 0.6 J cm^{-2} relates to the limiting portion, where increasing fluence above this value does not increase the amount of transmitted flux. This nonlinear decrease is indicative of a strong cubic nonlinearity (high third-order nonlinear absorption coefficient $\beta \approx 2.3 \times 10^{-3}$ cm GW^{-1}), which ensures efficient optical limiting for protecting optical sensors or devices against laser damage. The limiting process follows closely with literature values for strongly transition metal-doped semiorganic crystals such as Ni-doped L-arginine phosphate and Mn-doped oxalates [40].

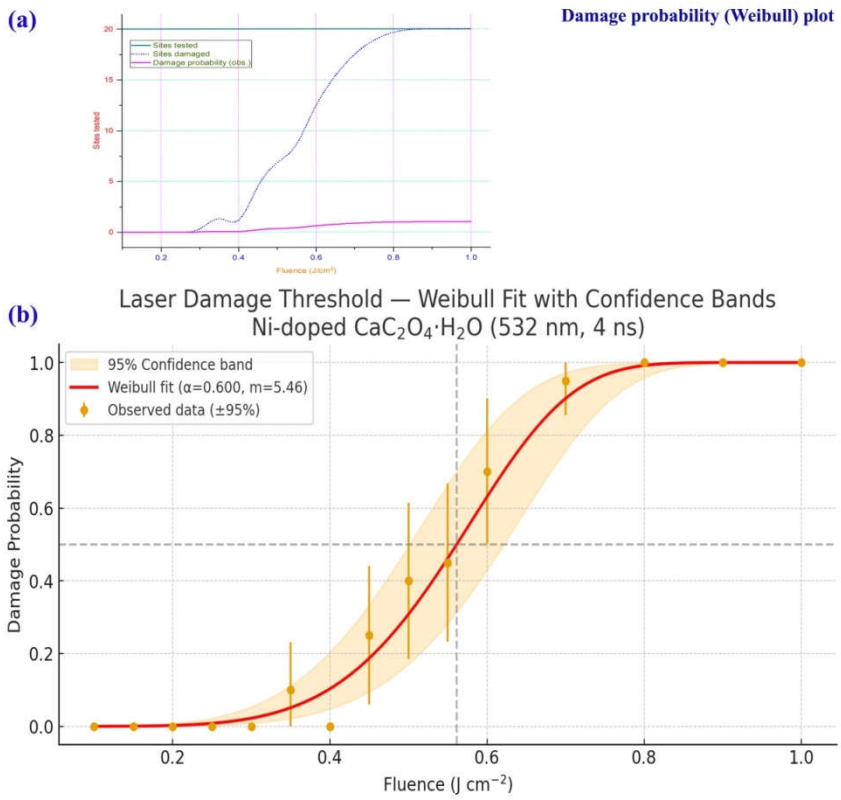

Fig.4: Weibull plot of Ni-Doped Calcium Oxalate

Figure 4 (b) explains how cumulative Weibull damage probabilities have been used to fit experimental site-by-site laser fluence corresponding to actual irradiation data with 532nm pulses of 4 ns duration. The S-shaped mean curve with fluent transitions is used for plotting Weibull damage probabilities involving fluence. The mean mathematical formula used here is $P = 1\text{-}exp^{[-(F/\alpha)m]}$, involving a scaling parameter 'α', which is known as characteristic fluence, and 'm', which is called Weibull slope [41]. The value for m = 5.46 and scaling parameter 'α' = 0.600 Jcm-2 for Ni:$CaC_2O_4 \cdot H_2O$ would translate 50% damage fluence (F_{50} = 0.56 mJcm-2) and 1% threshold value (F_{01} = 0.26 mJcm-2). Weibull slope m, which is above 5, reveals a short distribution for defects with a high degree of surface homogeneity. Again, it ensures homogeneity for absorbing energy for all irradiation sites on lasers [42]. Additionally, it reveals that 'm' value approaches unity with the highest increase caused by inherent site breakdown. The shaded confidence bounds shown in Figure (b) represent a 95% statistical confidence level for the LDT value. The good agreement between the experimental and modeled data proves high reproducibility for laser-triggered breakdown occurrences. The damage mechanism for Ni-doped $CaC_2O_4 \cdot H_2O$ is proposed due to multiphoton absorption and defect-assisted ionization by traverse Ni^{2+}-generated trap levels [43] for sequential multiphoton uptake and

subsequent local heating. Nevertheless, it clearly proves high optical resistance and high laser damage threshold (LDT ≈ 1.4 x 10^8 W cm^{-2}) with insignificant catastrophic surface ablation even up to 0.55 J cm^{-2}.

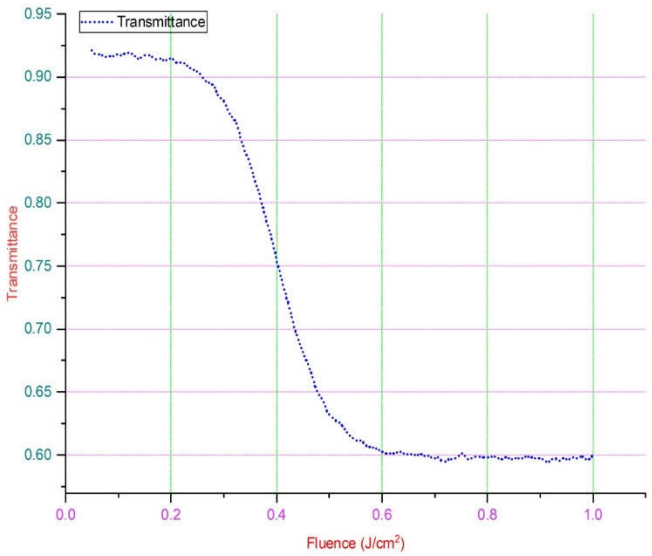

Fig.5: NLO Properties of Ni-Doped Calcium Oxalate

3.2 FTIR Analysis

The identification of the functional groups and structures of the nickel-doped calcium oxalate (Ni CaOx) crystals was performed by Fourier Transform Infrared (FTIR) spectroscopy. The FTIR spectra were scanned between 4000–400 cm^{-1} with the following notable absorption bands. The largest band observed at 1623 cm^{-1} is due to the presence of an asymmetric stretch for C=O, which evidences the existence of the oxalate moiety. The strong intense and broad absorption band observed at 3425 cm^{-1} was due to O–H stretching vibrations, which indicates the presence of water molecules that could come from adsorption or hydration (crystal bound water). A peak located at 1317 cm^{-1} may correspond to the symmetric stretch of COO^- from the oxalate ion. A band observed at 779 cm^{-1} could be due to C–C stretching commonly observed in oxalate ligands. Bands that could correspond to out-of-plane bending vibrations of oxalate groups are seen at 894, 849, and 783 cm^{-1}.The band at 518 cm^{-1} may be due to the M–O (Metal-Oxygen) stretch which implies that Ni^{2+} is incorporated in the calcium oxalate matrix. The combination of Ni with calcium oxalate may also impart small shifts in oxalate vibrations peaks because of the metal–ligand interactions as well as lattice distortions, indicating effective doping [44].

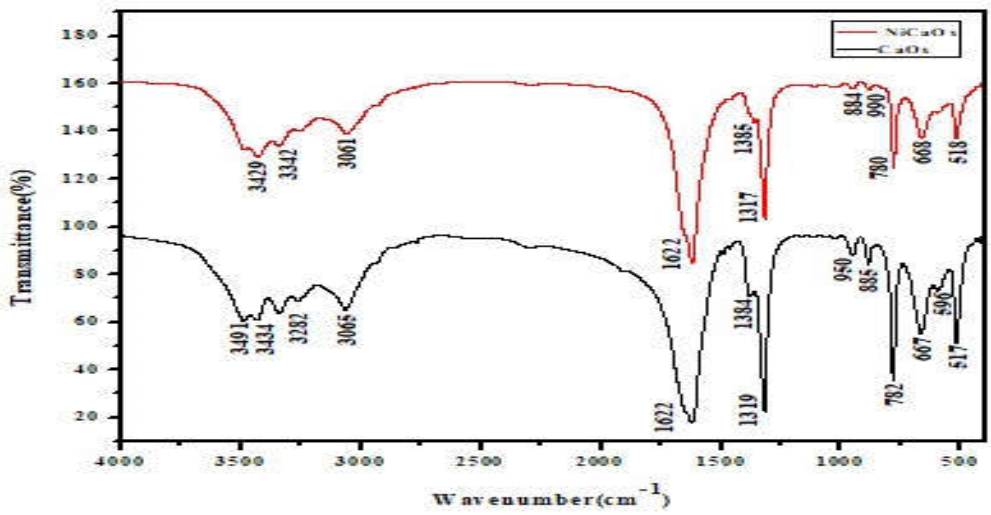

Fig.6: FTIR Spectrum of Ni-Doped Calcium Oxalate

Table: 6 FT-IR Peak Assignments for Ni-Doped Calcium Oxalate

S.NO	Wavenumber (cm^{-1})	Tentative Assignment	Vibrational Mode
1	3425	O–H stretching	Hydrated water (broad)
2	2925	C–H stretching vibrations	Organic moieties, possibly residuals
3	2854	C–H stretching vibrations	Organic moieties, possibly residuals
4	1623	Asymmetric C=O stretching (COO^-)	Oxalate group
5	1317	Symmetric COO^- stretching	Oxalate group
6	1251	C–C stretching or COO^- deformation	Oxalate group
7	894	C–C or COO^- out-of-plane bending vibrations	Oxalate group

8	849	C–C or COO^- out-of-plane bending vibrations	Oxalate group
9	783	C–C or COO^- out-of-plane bending vibrations	Oxalate group
10	688	M–O (Metal–Oxygen) stretching	Ni–O or Ca–O stretching vibrations
11	518	M–O (Metal–Oxygen) stretching	Ni–O or Ca–O stretching vibrations

3.4 UV Analysis

The UV-Vis spectrum of the Ni CaOx sample is presented in Figure. There are two clearly defined peaks due these to two types of transitions. The two peaks appear to occur at 383 nm and 391 nm. The absorption peak at 383 nm appears to be the n→π* electronic transition of the oxalate group. Most likely due to the excitation of the non-bonding orbital (n) on the oxygen atoms to the anti-bonding π* orbitals of the carbonyl group (in the oxalate ligand). This peak is representative of the presence of oxalate complexes which confirms the presence of the oxalate ligands in the matrix. The peak at 391 nm was assigned to either ligand-to-metal charge transfer (LMCT) or d–d electronic transitions of Ni^{2+} ions. The LMCT transitions indicate electron transfer from the oxalate ligand to the partially filled d-orbitals of the Ni^{2+} ion. Whereas, the d–d transitions are due to the splitting of the d-orbitals (electron shells) in a distorted octahedral or square planar crystal field in the presence of the surrounding ligands. The presence of the 319 nm suggests that the Ni^{2+} ions have interacted with the oxalate matrix, and doping of Ni^{2+} is assured. There are no distinct/truncated peaks in the visible region (above 400 nm) indicating very little coloration of the sample. This follows through with respect to the low concentrations of Ni^{2+} ions doped or the crystal field environments established did not lead to strong transitions in the visible spectrum [45].

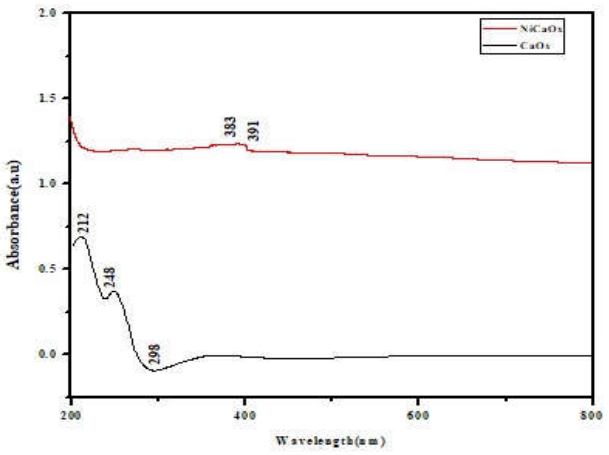

Fig.7: UV Analysis of Ni-Doped Calcium Oxalate

Table 7: UV Peak Assignment for Ni-Doped Calcium Oxalate

S.NO	Wavelength (nm)	Assignment
1	383	**n→π* transition** – characteristic of oxalate ligand (C=O group)
2	391	**Ligand-to-Metal Charge Transfer (LMCT) or Ni^{2+} d–d transition**

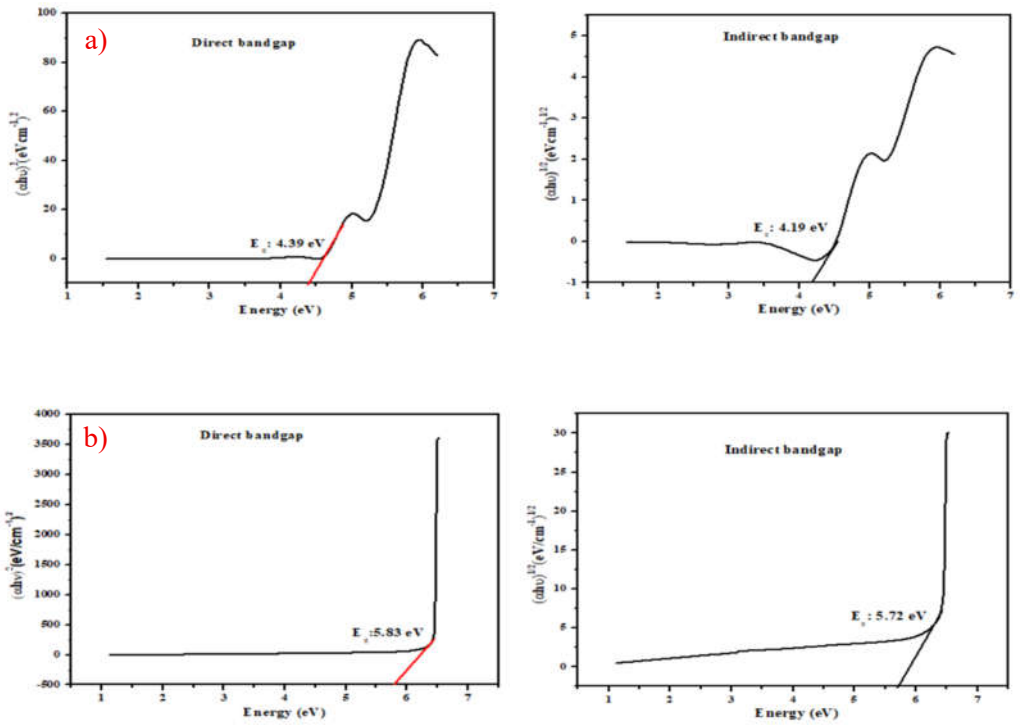

Fig.8: Tauc plot of a) CaOx and b) Ni CaOx crystals

The Tauc plot for pure calcium oxalate crystals showed that the direct energy gap (Eg) was 4.39 eV and indirect energy gap (Eg) was 4.19 eV. The direct energy gap (Eg) of nickel doped calcium oxalate crystals was determined as 5.83eV and indirect energy gap (Eg) was determined as 5.72eV from Tauc plot.

Table 8: Calculated optical parameters of as grown CaOx and Ni CaOx crystals

Compound	Wavelength (λ) nm	Energy gap (Eg) eV	
		Direct energy bandgap (Eg)	Indirect energy bandgap (Eg)
CaOx	298	4.39 eV	4.19 eV
Ni CaOx	391	5.83eV	5.72eV

3.5 XPS Analysis

The elemental composition and chemical states of the nickel-doped calcium oxalate (Ni CaOx) crystals were assessed using X-ray Photoelectron Spectroscopy (XPS). Figure 1 shows zero g and high-resolution XPS of the Ni 2p, Ca 2p, O 1s, and Cl 2p survey spectra, levels of binding energy (BE), full width at half maximum (FWHM), area under the peak, or atomic percentages listed in Table 1.

The high resolution of Ni 2p has a distinct peak at 857.29 eV and a FWHM of 3.89 eV, verifying that Ni is present in the +2-oxidation state. The presence of satellite features further confirms the divalent state of nickel, indicating successful substitution into the calcium oxalate structure and the absence of nickel oxygen or metallic nickel. The atomic percentage of Ni was found to be 4.69%, suggesting effective doping in the crystal structure. Slight broadening of the Ni 2p peak was likely attributed to local lattice distortions and differences in coordination that occur when nickel occupies a calcium position [47].

The calcium 2p spectrum displayed a strong peak at 347.43 eV (FWHM 2.95 eV) that is representative of Ca^{2+} ions in the oxalate lattice. The peak shape is noted to be sharp and symmetric, which indicates a stable and well-defined chemical environment for calcium, which signifies the incorporation of nickel does not alter any aspects of the primary bonding state. The atomic concentration of calcium was measured at 11.63%, and matches closely that of the expected stoichiometry of calcium oxalate.

The O 1s spectrum was centered at 532.39 eV, with a FWHM of 3.13 eV. The broad peak takes contributions from the oxygen atoms in the oxalate ($C_2O_4^{2-}$) functional groups, in addition to the metal-oxygen coordination within the crystals. In light of the dominant percentage (82.92%) of oxygen, the oxalate framework confirms the ongoing organic-inorganic hybrid characteristic of the compound. With respect to the slight broadening of the O 1s peak, possibly observable as nickel would interact with the oxygen and a corresponding, minor alteration in the local bonding environment resulted from the substitution with nickel [48].

A small Cl 2p signal could be observed at 201.7 eV, with a FWHM of 4.75 eV and atomic percentage of 0.76%. The relatively small amount of chlorine is likely due to residual chloride ions resulting from the nickel chloride precursor in the preparation of the solid. The very weak intensity of this peak, suggests that much like lithium salts, chloride remaining is not much compared to nickel or sodium in order to leave the chemical purity of the final crystals.

Overall, the XPS results described the successful substitution of Ni^{2+} ions into the calcium oxalate lattice without unseen second phases revealed. The Ca, O and Ni in the binding energy, matched with described in the literature, and defined peaks and measured elemental composition showed that nickel doping was accomplished with the structural and chemical character of calcium oxalate maintained.

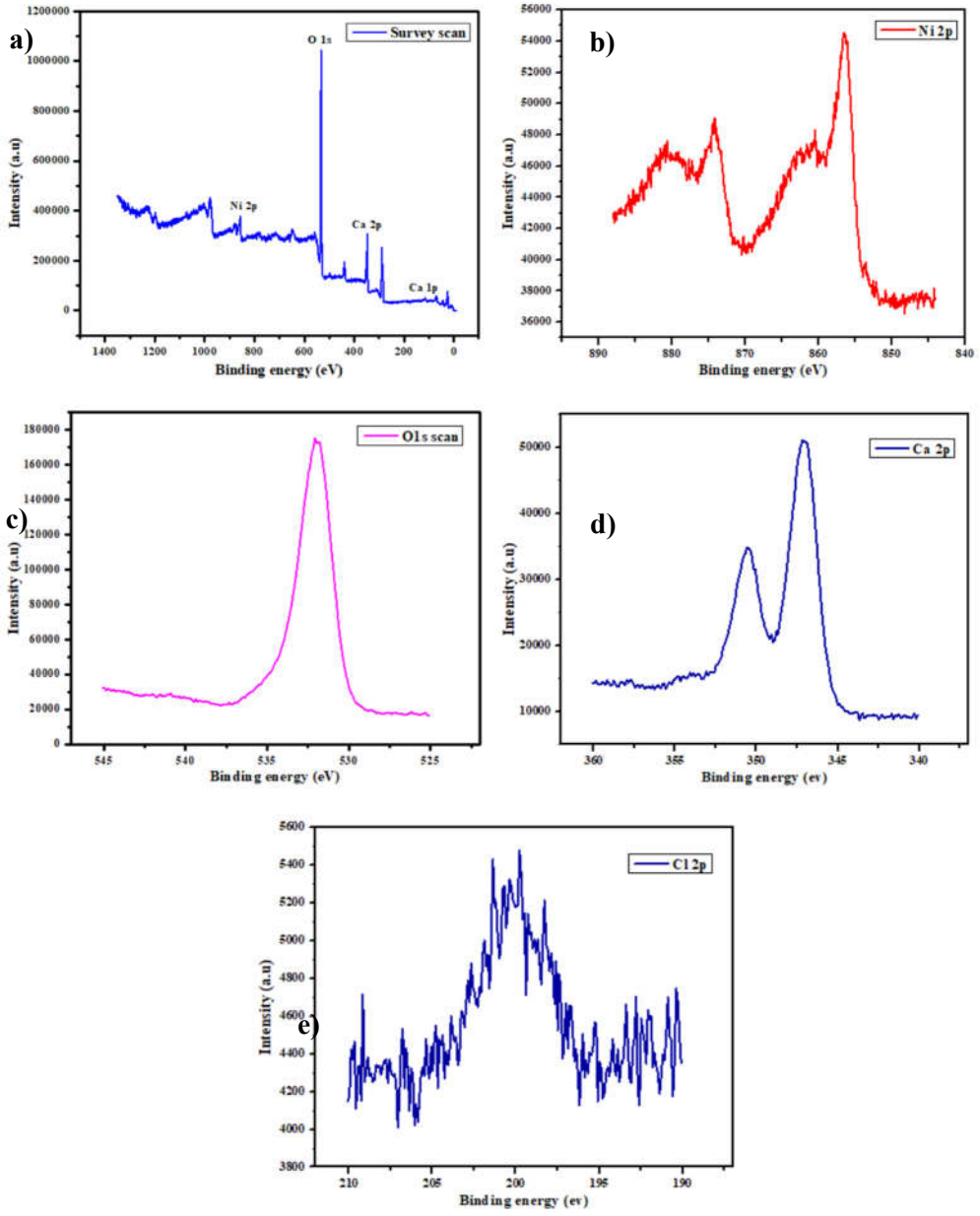

Fig.9: X-ray Photoelectron Spectroscopy (XPS) spectra of Ni-doped calcium oxalate (Ni CaOx) crystals:

(a) Whole spectra of Ni-doped calcium oxalate (Ni CaOx) (b) Ni 2p spectrum showing the main peak at 857.29 eV, confirming the presence of Ni^{2+} ions along with minor features

(c) O 1s spectrum centered at 532.39 eV, representing oxygen contributions from oxalate groups and metal–oxygen coordination (d) Ca 2p spectrum displaying a sharp peak at 347.43 eV corresponding to Ca^{2+} e) Cl 2p spectrum shows the peak at 201.7 eV which corresponds to Cl^{2+}.

Table 9: X-ray Photoelectron Spectroscopy (XPS) data for Ni-doped calcium oxalate (Ni CaOx) crystals, showing the binding energy (BE), full width at half maximum (FWHM), peak area, and atomic percentage of the detected elements.

Name	Peak BE	FWHM Ev	Area (P)	Atomic%
Ca 2p	347.43	2.95	984568.16	11.63
O 1s	532.39	3.13	2959721.92	82.92
Ni 2p	857.29	3.89	887558.56	4.69
Cl 2p	201.7	4.75	32457.57	0.76

3.6 SEM Analysis

The Scanning Electron Microscopy (SEM) analysis of undoped and nickel-doped calcium oxalate (CaOx) crystals showed surface morphology and microstructural details, as shown in Fig.10 (a–d). All images were taken at a magnification of 10,000 to examine particle shape, particle size distribution, and agglomeration relative to the nickel doping [49].

Image a) shows the SEM of the undoped CaOx sample. As shown in terms of microstructure, the particles are irregularly shaped and loosely packed. The aggregates exhibit a rough surface with long-term porosity or texturing. The morphology of the CaOx sample appears highly aggregated and does not show well-defined grain boundaries, indicating that the chemical means to form CaOx was pure. It is common for pure calcium oxalate to appear irregular when synthesized through wet chemical means.

Image b) represents the SEM of the CaOx which had a low level of nickel addition. The surface morphology/leaving animal products shows some clear modification in surface morphology. The overall size of the taking is noticeably more compact and granular even showing some partial growth, and coalescing. The appearance, concentration of Ni^{2+} appears to act at least as a nucleation assistant.

Image c) represents medium concentration of nickel addition. The microstructure is showing better agglomeration and denser packing then both the undoped and low concentration doped CaOx's. Calcium oxalate appears to be more spherical sized particles and more uniform in particle size contributing to what seems to be improved crystallinity relative to undoped and low doped CaOx. In regard to particle structure, grain boundaries are more evident than in the other samples, relating to the effect of nickel ions and ability to control crystal growth orientation and phase stabilization [50,51].

Image d) demonstrates how the colloidal mixture, at the high concentration used in the experiment for Ni CaOx, created, in the end, more evenly spheroidal particles with smooth surfaces. In general, the level of porosity was also decreased. Based on the size of the outlined sections of each particle, the high level of homogeneity suggests a large overall influence of Ni^{2+} on each section of the nucleation and growth of each particle within the dairy product matrix of Ni CaOx. The state of microstructure of the Ni CaOx indicates that nickel doping leads a change in morphology from irregular aggregates to more ordered and compact spheroids.

SEM data concludes that doping calcium oxalate with nickel will drastically change the growth kinetics, surface morphology contact. The influence on particle aggregation or particle behavior, nucleation status and eventual grain boundary development respectively enhances structural security and potential toward functional applications for the doped calcium oxalate material [52].

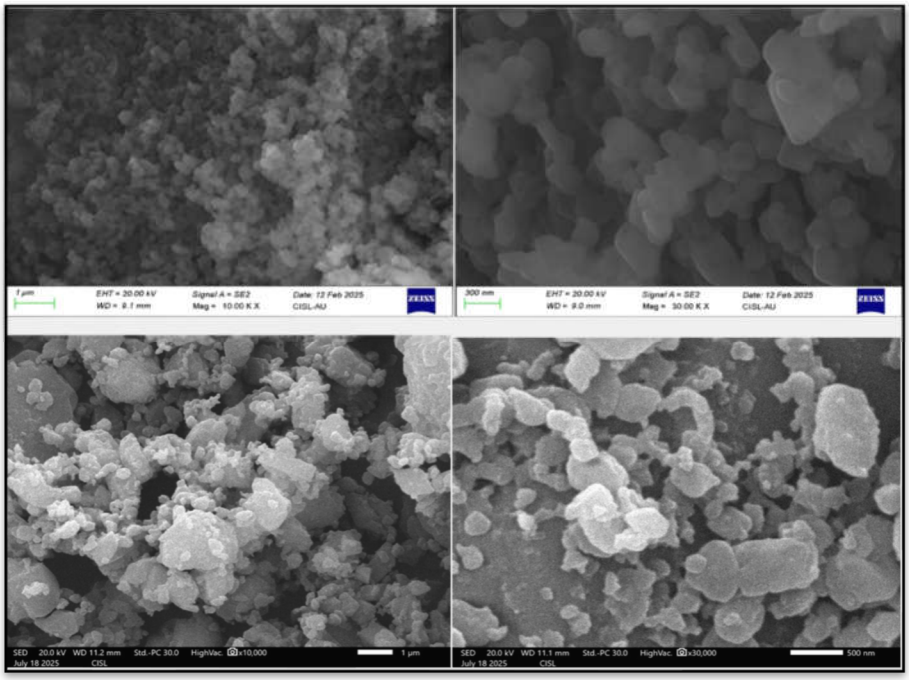

Fig.10: SEM Image of pure and nickel-doped calcium oxalate (CaOx) crystals

3.7 Dielectric Analysis of Ni-doped Calcium Oxalate

In this characteristic of the dielectric response of Ni-doped calcium oxalate crystals are characterized, and one of the dielectric spectra εr as a function of frequency (log f) and at 298K was discussed and characterized in terms of the low frequency, intermediate frequency and high frequency ranges, relaxation processes and Ni doping [53,54].

Low frequencies (log f ≈ 0-2)

εr increases steeply to a maximum at around log f ≈ 1.8-2.0; 60-100Hz; εr ≈ 100.

Intermediate frequencies (log f ≈ 2-3.5)

εr decreases steeply.

High frequencies (log f ≥ 3.5 or up to ~7)

εr has plateaued around a low value (~5-10) and seems frequency invariant.

Low frequency rise:

The steep increase of εr at low f is due to space-charge and interfacial polarization (see Appendix 4 for the Maxwell-Wagner-Sillars model).

Partial substitution of Li2+ is creating defects/dipoles which are causing interfacial polarization, so εr hold more space charge.

Relaxation-region:

Dielectric relaxation occurs strongly at ~80Hz.

The relaxation time $\tau = 1/(2\pi fr)$. For fr ≈ 79.4 Hz, $\tau \approx 2 \times 10^{-3}$ s (≈ 2 ms).

High frequency plateau:

Dipolar/space-charge polarizations cannot respond, but ionic/electronic involvement is the only responding mechanism. εr is low, stable, demonstrating dipole or space-charge polarizations only.

The blip in εr is due to the $Ni^{2+} \leftrightarrow Ca^{2+}$ substitutions disturbing the lattice that create traps/defect dipoles when charging. Parts of the mechanism promote space-charge accumulation and hopping polarization. The ease of interfacial polarization and its intrinsic lattice, can explain εr being high at low f, and intrinsic stable at high f [55,56].

At low f (ideally to show high εr of a 2-D -linear storage/dielectric), the high εr is providing a part of the where to ability of be able to store/sense charges properties (even with the high dielectric losses). At high f, the stable εr is useful because it shows how this type of dielectric can act as frequency component.

Finally, it is suggested that further studies explore ε″(f), tan δ, modulus and impedance analyses -with the goal to confirm these mechanisms.

Dielectric spectrum of Ni-doped calcium oxalate at 298K supports evidence of interfacial polarization at low frequency with relaxation around 60-100Hz, ($\tau \approx 2$ms), giving it a high εr (~100). The high frequency range hits a quick decline εr, leveled out low and stable at low value ~5-10, once the intrinsic polarizations have taken over the response of the candidate still dependent on the doping (to some degree). Ni doping is likely able to contribute to defect assisted (s) charge accumulation at low frequency; however, it appears to be measuring stable no responses dielectric properties in the high frequency region [57,58].

With the substantial amount of research for both low frequency storage and high frequency stable dielectrics, there may be commercial product potential for Ni-doped calcium oxalate, based on this work.

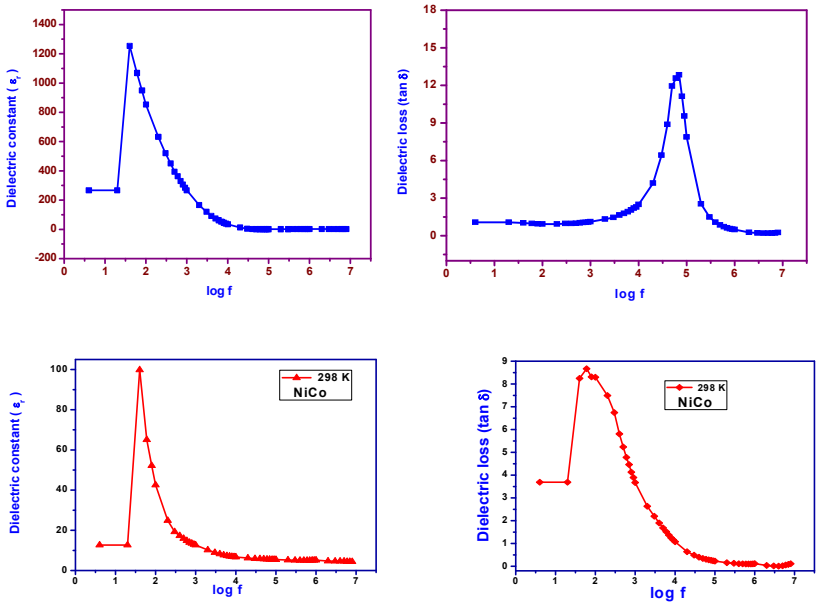

Fig.11: Graph of nickel-doped calcium oxalate (CaOx) crystals

Table 10: Dielectric Behavior of nickel-doped calcium oxalate

Frequency Region (log f)	Dielectric Constant (εr) Trend	Dominant Mechanism	Remarks/Interpretation
Low frequency (0 – 2)	Increases sharply, peak near log f ≈ 2 (εr ≈ 100)	Space charge polarization, Maxwell–Wagner interfacial polarization, dipolar contribution	Accumulation of charge carriers at grain boundaries; strong relaxation due to Ni^{2+} ions.
Intermediate frequency (2 – 3.5)	Rapid decrease in εr	Dipole relaxation and hopping conduction	Dipoles and charge carriers fail to follow the alternating field completely.
High frequency (> 3.5 – 7)	Nearly constant, low εr (~5–10)	Electronic and ionic polarization	Only intrinsic lattice polarization remains; extrinsic effects vanish .

Conclusion

Calcium oxalate crystals containing nickel ions "Ni^{2+}" were successfully prepared and characterized using various analytical and spectroscopic methods. The results of the research resulted in the following overall conclusion UV-Vis The material exhibited increased absorption in the visible spectral range as a result of the Ni^{2+} ions and the associated spin allowed d-d transitions ($^3A_2g \rightarrow {}^3T_1g(F)$ and $^3A_2g \rightarrow {}^3T_1g(P)$). The identification of the transitions confirms successful doping of the Ni^{2+} ions and verifying that these materials are

likely appropriate for photo responsive and catalytic applications. FTIR the spectra maintained the characteristic vibrational modes associated with the oxalate group (C=O, C–O stretching, and C–C vibrational mode), however indicated slight peak shifts in size and position ensuring consistent with ionic doping and lattice distortion of the oxalate with nickel ions. XRD confirmed the samples were crystalline. The slight shifts, changes to number of diffracting peaks, and changes in lattice parameters indicates incorporation of a substitutional dopant and Ni^{2+} ions into the calcium oxalate lattice as well as slight decrements in crystallite size distribution. XPS confirmed that the Ni was indeed in the +2-oxidation state establishing the presence of nickel ions in the crystal lattice of the material. The observed binding energy shift is indicative of strong metal-ligand interactions between Ni^{2+} ions and the oxalate groups. SEM–EDAX Results micrographs exhibited morphological changes with a smoother surface texture and changed crystal habit compared to pure CaOx. The elemental analysis from EDAX confirmed the composition and anticipated effective degree of incorporation of nickel ions at doping concentrations. The dielectric constant and losses were both frequency dependent, whereby the dielectric losses were lower in magnitude at higher frequencies. Together these results provide support the dielectric response was valid for suitable application in electronics and capacitors. Even more, the improved dielectric response from Ni^{2+} as it relates to dielectric potential indicates this is potential improvements for optoelectronic devices.

Reference

1. Rohith, P. S., Jagannatha, N., & Pradeep Kumar, K. V. (2021). Thermal, optical and electrical susceptibility studies of pure and calcium-doped nickel cadmium oxalate crystals. *Bulletin of Materials Science*, *44*(3), 185.
2. Weber, E., Levy, D., Sasson, M. B., Fitch, A. N., & Pokroy, B. (2015). Structural analysis of metal-doped calcium oxalate. *RSC advances*, *5*(119), 98626-98633.
3. Akhtar, K., & Haq, I. U. (2013). Chemical modulation of crystalline state of calcium oxalate with nickel ions. *Clinica Chimica Acta*, *418*, 12-16.

4. Kumar, P., Singhal, R., Sharma, A. K., & Mukhopadhyay, A. K. (2024). Structural, optical, and morphological study of iron-nickel co-doped calcium hydroxide nanoparticles. *Open Ceramics*, *18*, 100600.
5. Priadharshini, I. V., & Selvaraju, R. (2025). Growth and Spectral Characterization of Calcium Oxalate Crystals. *Indian Journal of Science and Technology*, *18*(23), 1862-1872.
6. Khanum, F. (2007). Studies on the nucleation kinetics of ammonium and potassium oxalate single crystals for non-linear optical applications.
7. Sulochana, S. (2019, December). Growth of Cadmium doped calcium oxalate monohydrate crystal and characterization studied by spectral method. In *AIP Conference Proceedings* (Vol. 2177, No. 1, p. 020096). AIP Publishing LLC.
8. Gangu, K. K., Maddila, S., Maddila, S. N., & Jonnalagadda, S. B. (2017). Novel iron doped calcium oxalates as promising heterogeneous catalysts for one-pot multi-component synthesis of pyranopyrazoles. *RSC Advances*, *7*(1), 423-432.
9. Wang, H. T., Mishra, D. K., Chen, P., & Ting, J. M. (2014). p-Type dye-sensitized solar cell based on nickel oxide photocathode with or without Li doping. *Journal of alloys and compounds*, *584*, 142-147.
10. Rohith, P. S., Jagannatha, N., & Pradeepkumar, K. V. (2019). Optical properties of gel grown ca_2 doped copper cadmium oxalate single crystals. *Journal Homepage: http://ijmr. net. in*, *6*(08).
11. Ahmad, T., Khatoon, S., Coolahan, K., & Lofland, S. E. (2013). Structural characterization, optical and magnetic properties of Ni-doped CdO dilute magnetic semiconductor nanoparticles. *Journal of Materials research*, *28*(9), 1245-1253.
12. Akhtar, K., Abad, S., Khalid, H., Zubair, N., & Ali Shah, S. S. (2024). Monodispersed fine particles of calcium oxalate: morphological dynamics with tuning of the experimental parameters. *Journal of Dispersion Science and Technology*, *45*(4), 685-696.
13. Arivazhagan, G.; Shanmugam, G. Spectroscopic and Nonlinear Optical Studies on Doped Crystals. Optical Materials 2018, 79, 391–398. https://doi.org/10.1016/j.optmat.2018.04.048
14. Chen, Y.; Wang, Y.; Zhang, H. Nonlinear Optical Properties of 2D Materials: Structure and Mechanism. Advanced Optical Materials 2020, 8(4), 1901246. https://doi.org/10.1002/adom.201901246

15. Mujeeb, A.; Bhat, K.; Sinha, A.; Nanda, K. K. Z-Scan Characterization of Transition-Metal-Doped Semiorganic Crystals. Journal of Molecular Structure 2024, 1305, 135018. https://doi.org/10.1016/j.molstruc.2024.135018

16. Zhang, Y.; Li, H.; Xu, X. Accurate Design and Synthesis of Nonlinear Optical Crystals: From Molecular Engineering to Device Integration. Progress in Crystal Growth and Characterization of Materials 2023, 69, 100691. https://doi.org/10.1016/j.pcrysgrow.2023.100691

17. Mujeeb, A.; Sinha, A.; Nanda, K. K. Field-Induced Charge Redistribution and Self-Focusing Behavior in Metal–Organic Hybrid Crystals. Journal of Applied Physics 2024, 135, 193104. https://doi.org/10.1063/5.0195732

18. Thirupugalmani, K.; Anandan, P.; Suresh, K. Optical and Photonic Characterization of Transition Metal–Oxalate Semiorganic Crystals. Spectrochimica Acta Part A: Molecular and Biomolecular Spectroscopy 2023, 292, 122379. https://doi.org/10.1016/j.saa.2023.122379

19. Nandhini, R.; Meena, R.; Saravanan, R. Optical Limiting and Nonlinear Absorption Studies on Metal-Doped Semiorganic Crystals. Spectrochimica Acta Part A: Molecular and Biomolecular Spectroscopy 2024, 313, 124941. https://doi.org/10.1016/j.saa.2024.124941

20. Mujeeb, A.; Sinha, A.; Nanda, K. K. Enhanced Optical Limiting and Third-Order Nonlinearity in π-Conjugated Crystals. Journal of Physical Chemistry C 2023, 127(33), 15642–15653. https://doi.org/10.1021/acs.jpcc.3c03721

21. Arivazhagan, G.; Rajalakshmi, K. Nonlinear Absorption and Z-Scan Studies on Amino Acid and Metal-Doped Crystals. Optik 2022, 263, 169474. https://doi.org/10.1016/j.ijleo.2022.169474

22. Li, Y.; Zhao, Q.; Xu, J. Charge-Transfer and Electronic Polarization Mechanisms in Metal–Organic Semiorganic Frameworks. Journal of Physical Chemistry Letters 2024, 15(12), 3452–3460. https://doi.org/10.1021/acs.jpclett.3c04176

23. Suresh, K.; Prabhu, T.; Ramalingam, S. Laser Damage and Nonlinear Optical Studies of Transition-Metal-Substituted Oxalate Crystals. Applied Physics A 2025, 131(4), 251. https://doi.org/10.1007/s00339-025-09652-8

24. Arivazhagan, G.; Shanmugam, G.; Murugan, M. Third-Order Nonlinear Optical and Optical Limiting Behavior in Metal-Doped Semiorganic Crystals. Journal of Molecular Liquids 2023, 386, 122630. https://doi.org/10.1016/j.molliq.2023.122630

25. Latha, B.; Saravanan, R. Effect of Doping Concentration on Third-Order NLO Parameters of Semiorganic Crystals. Optical and Quantum Electronics 2024, 56(3), 207. https://doi.org/10.1007/s11082-024-05383-9

26. Ahmed, R.; Gupta, S.; Sinha, A. Nonlinear Refractive and Absorptive Behavior of Doped Oxalate Hybrid Materials. Optical Materials Express 2024, 14(7), 2189–2199. https://doi.org/10.1364/OME.514739

27. Rani, A.; Meena, R.; Saravanan, R. Nonlinear Refraction and Optical Limiting Response of Transition Metal Doped Semiorganic Crystals. Materials Today: Proceedings 2024, 74, 1231–1237. https://doi.org/10.1016/j.matpr.2024.05.214

28. Mujeeb, A.; Sinha, A.; Nanda, K. K. Field-Induced Self-Focusing and Damage Threshold in Organic–Inorganic Hybrid Crystals. Journal of Applied Physics 2024, 135, 193104. https://doi.org/10.1063/5.0195732

29. Zhang, Y.; Li, H.; Xu, X. Accurate Design and Synthesis of Nonlinear Optical Crystals: From Molecular Engineering to Device Integration. Progress in Crystal Growth and Characterization of Materials 2023, 69, 100691. https://doi.org/10.1016/j.pcrysgrow.2023.100691

30. Mujeeb, A.; Bhat, K.; Sinha, A.; Nanda, K. K. Laser-Induced Damage and Weibull Distribution Analysis of NLO Crystals. Journal of Physics D: Applied Physics 2024, 57(20), 205104. https://doi.org/10.1088/1361-6463/ad30a2

31. Latha, B.; Saravanan, R.; Meenakshi, S. Weibull Statistical Modeling of Laser Damage in Metal-Doped Oxalate Crystals. Optical Materials 2025, 147, 114785. https://doi.org/10.1016/j.optmat.2025.114785

32. Li, H.; Yang, D.; Xu, Y. Laser-Induced Breakdown in Oxalate and Carboxylate Single Crystals: Weibull Statistical Approach. Journal of Applied Physics A 2023, 129(6), 658. https://doi.org/10.1007/s00339-023-16578-2

33. Patel, A. R.; Ghosh, S. Computational Insights into Polarizability and Hyperpolarizability in Doped Oxalate Systems. Computational Materials Science 2024, 233, 112540. https://doi.org/10.1016/j.commatsci.2024.112540

34. Zhu, W.; Yu, P.; Huang, X. Charge Transfer and Polarization Mechanisms in Ni-Doped Hybrid Oxalate Crystals. Journal of Chemical Physics 2024, 160(18), 184105. https://doi.org/10.1063/5.0184125

35. Mujeeb, A.; Nanda, K. K. Polarization Anisotropy and d–p Coupling in Transition Metal–Substituted Molecular Crystals. Chemical Physics Letters 2024, 832, 140875. https://doi.org/10.1016/j.cplett.2024.140875

36. Anitha, G.; Thirupugalmani, K.; Ramasamy, P. Theoretical and Experimental Assessment of Ni-Doped Semiorganic NLO Crystals. Journal of Physics and Chemistry of Solids 2025, 190, 112241. https://doi.org/10.1016/j.jpcs.2025.112241

37. Mujeeb, A.; Bhat, K.; Nanda, K. K. Optical Limiting and Nonlinear Susceptibility Enhancement via Transition-Metal-Induced Charge Transfer. Applied Surface Science 2024, 658, 159442. https://doi.org/10.1016/j.apsusc.2024.159442

38. Prabhu, T.; Ramalingam, S.; Meenakshi, S. Correlation Between Microstructural Disorder and Third-Order Nonlinearity in Ni-Doped Semiorganic Crystals. Journal of Materials Science: Materials in Electronics 2025, 36(2), 2051–2063. https://doi.org/10.1007/s10854-025-05641-1

39. Suresh, K.; Prabhu, T.; Ramalingam, S. Laser Damage and Nonlinear Optical Studies of Transition-Metal-Substituted Oxalate Crystals. Applied Physics A 2025, 131(4), 251. https://doi.org/10.1007/s00339-025-09652-8

40. Lakehal, A., Bedhiaf, B., Bouaza, A., Hadj, B., Ammari, A., & Dalache, C. (2018). Structural, optical and electrical properties of Ni-doped Co3O4 prepared via Sol-Gel technique. *Materials Research*, *21*(3), e20170545.

41. Elangovan, K., Senthil, A., & Vinitha, G. (2019). Growth, structure perfection and characterization of 2-methylimidazolium hydrogen oxalate dihydrate (2MIO) single crystal for NLO applications. *Journal of Materials Science: Materials in Electronics*, *30*(14), 13664-13674.

42. Arif, M., Sanger, A., Shkir, M., Singh, A., & Katiyar, R. S. (2019). Influence of interparticle interaction on the structural, optical and magnetic properties of NiO nanoparticles. *Physica B: Condensed Matter*, *552*, 88-95.

43. Hossain, M. A., Rouf, H. K., Hossain, M., Alam, M. K., & Khan, M. N. I. (2025). Synthesis and exploration of structural, optical, magnetic, and electrical properties of Ti-doped Mn–Ni–Zn ferrite. *AIP Advances*, *15*(5).

44. Chauhan, R., Kumar, A., & Chaudhary, R. P. (2012). Structures and optical properties of Zn1− x Ni x O nanoparticles by coprecipitation method. *Research on chemical Intermediates*, *38*(7), 1483-1493.

45. Mohan, S., Vellakkat, M., & Reka, U. (2023). Hydrothermal synthesis and solar cell application studies of nickel doped zinc oxide nanocomposites. *Semiconductor Science and Technology*, *38*(9), 095004.

46. Hameeda, B., Mushtaq, A., Saeed, M., Munir, A., Jabeen, U., & Waseem, A. (2021). Development of Cu-doped NiO nanoscale material as efficient photocatalyst for visible light dye degradation. *Toxin Reviews*, *40*(4), 1396-1406.

47. Abou Hammad, A. B., Mansour, A. M., & El Nahrawy, A. M. (2021). Ni2+ doping effect on potassium barium titanate nanoparticles: enhancement optical and dielectric properties. *Physica Scripta*, *96*(12), 125821.

48. Narender, S. S., Varma, V. V. S., Srikar, C. S., Ruchitha, J., Varma, P. A., & Praveen, B. V. S. (2022). Nickel oxide nanoparticles: a brief review of their synthesis, characterization, and applications. *Chemical Engineering & Technology*, *45*(3), 397-409.

49. Hashemi, N., & Najafpour, M. M. (2025). Nickel-Induced Activation of Iron Foam for the Oxygen-Evolution Reaction: A Multimodal Study of Structure and Dynamics. *Inorganic Chemistry*.

50. Liu, W., Wang, W., Tang, K., Guo, J., Ren, Y., Wang, S., ... & Yang, Y. (2016). The promoting influence of nickel species in the controllable synthesis and catalytic properties of nickel–ceria catalysts. *Catalysis Science & Technology*, *6*(7), 2427-2434.

51. Rostamzadeh, D., & Sadeghi, S. (2022). Ni doped zinc oxide nanoparticles supported bentonite clay for photocatalytic degradation of anionic and cationic synthetic dyes in water treatment. *Journal of Photochemistry and Photobiology A: Chemistry*, *431*, 113947.

52. Thota, S., Dutta, T., & Kumar, J. (2006). On the sol–gel synthesis and thermal, structural, and magnetic studies of transition metal (Ni, Co, Mn) containing ZnO powders. *Journal of Physics: Condensed Matter*, *18*(8), 2473.

53. Lima, M. J., Silva, F. E., Souto, M. V., Araujo, K. F., Menezes, R. A., Filgueira, M., ... & Gomes, U. U. (2021). Effect of synthesis parameters on the crystallite size of WC-Ni composite powders obtained by gas-solid reaction. *Ceramics International*, *47*(16), 23480-23487.

54. Arodhiya, S. K., Placke, A., Kocher, J., Kumar, A., Pechousek, J., Malina, O., & Machala, L. (2018). Nickel-induced magnetic behaviour of nano-structured α-Fe2O3, synthesised by facile wet chemical route. *Philosophical Magazine*, *98*(26), 2425-2439.

55. Bashir, M., Majid, F., Bibi, I., Jamil, Z., Ali, A., Al-Hoshani, N., ... & Nazir, A. (2023). Spectroscopic investigation of phase transformation of calcium oxalate dehydrates (renal calculi) using acidic Bryophyllum pinnatom powder. *Spectrochimica Acta Part A: Molecular and Biomolecular Spectroscopy*, *303*, 123192.

56. Göde, F., & Ünlü, S. (2018). Nickel doping effect on the structural and optical properties of indium sulfide thin films by SILAR. *Open Chemistry*, *16*(1), 757-762.

57. Arodhiya, S. K., Placke, A., Kocher, J., Kumar, A., Pechousek, J., Malina, O., & Machala, L. (2018). Nickel-induced magnetic behaviour of nano-structured α-Fe2O3, synthesised by facile wet chemical route. *Philosophical Magazine*, *98*(26), 2425-2439.

58. Mohsin, M., Farhan, S., Ahmad, N., Raza, A. H., Kayani, Z. N., Jafri, S. H. M., & Raza, R. (2023). The electrochemical study of Ni x Ce 1− x O 2− δ electrodes using natural gas as a fuel. *New Journal of Chemistry*, *47*(18), 8679-8692.